IOP Publishing Nanotechnology

Nanotechnology **28** (2017) 455707 (10pp) https://doi.org/10.1088/1361-6528/aa8b29

Hydrothermal synthesis of SnQ (*Q*=Te, Se, S) and their thermoelectric properties

Dan Feng[1,2], Zhen-Hua Ge[3], Yue-Xing Chen[2], Ju Li[1,4,5] and Jiaqing He[2,5]

[1] State Key Laboratory for Mechanical Behavior of Materials and Frontier Institute of Science and Technology, Xi'an Jiaotong University, Xi'an 710049, People's Republic of China
[2] Shenzhen Key Laboratory of Thermoelectric Materials, Department of physics, South University of Science and Technology of China, Shenzhen 518055, People's Republic of China
[3] Faculty of Materials Science and Technology, Kunming University of Science and Technology, Kunming, 650093, People's Republic of China
[4] Department of Nuclear Science and Engineering and Department of Materials Science and Engineering, Massachusetts Institute of Technology, Cambridge, MA 02139, United States of America

E-mail: liju@mit.edu and he.jq@sustc.edu.cn

Received 23 June 2017, revised 6 September 2017
Accepted for publication 8 September 2017
Published 16 October 2017

Abstract

Lead-free *IV–VI* semiconductors SnQ (Q = Te, Se, S) are deemed as promising thermoelectric (TE) materials. In this work, we designed a hydrothermal route to selectively synthesize single phase SnTe, SnSe and SnS nanopowders. For all three samples, the phase structure were characterized by x-ray diffraction, SnTe particles with octahedron structure and SnSe/SnS particles with plate-like shape were observed by field emission scanning electron microscopy and transmission electron microscopy, the formation mechanism was discussed in detail. Then, SnTe, SnSe and SnS nanopowders were densified by spark plasma sintering for investigating TE properties. It was noticed that SnSe and SnS exhibited remarkably anisotropy in both electrical and thermal properties attributed to the layered crystal structure. The highest ZT values 0.79 at 873 K, 0.21 at 773 K, and 0.13 at 773 K were achieved for SnTe, SnSe and SnS bulk samples, respectively.

Supplementary material for this article is available online

Keywords: SnQ (Q = Te, Se, S), thermoelectrics, hydrothermal method

(Some figures may appear in colour only in the online journal)

1. Introduction

Thermoelectric (TE) power generator is regarded as a promising technology due to the capability on generating electricity from waste heat [1, 2]. The conversion efficiency of a TE device is determined by the dimensionless figure of merit (ZT) defined as ZT = $S^2\sigma T/(\kappa_e + \kappa_l)$, where S, σ, κ_e, κ_l, and T are the Seebeck coefficient, electrical conductivity, electronic thermal conductivity, lattice thermal conductivity, and operating temperature, respectively. Approaches employed to enhance the ZT value can be concluded as electrical properties optimization, such as resonant doping [3], band convergence [4], modulation doping [5], etc, and lattice thermal conductivity reduction, such as nano-structuring [6–8], solid solution [9], all-scale hierarchical structuring [10], etc. Among all those TE materials, *IV–VI* semiconductors lead chalcogenides [11–14], PbTe in particular, exhibit the best TE performance in the moderate temperature range (~300–700 K). However, the practical application is seriously limited by the toxicity of Pb element. Therefore, the lead-free *IV–VI* semiconductor members, tin telluride (SnTe), tin selenide (SnSe) and tin sulfide (SnS), have been investigated as TE materials widely, and deemed as promising TE materials [15–20].

The crystal structure of SnTe, SnSe and SnS are shown in figure 1. SnTe performs a cubic structure with the $Fm\bar{3}m$ space group (PDF #46-1210), while SnSe and SnS possess an orthorhombic layered structure with the *Pnma* space group (PDF #48-1224 and PDF #39-0354) at room temperature,

---

[5] Authors to whom any correspondence should be addressed.

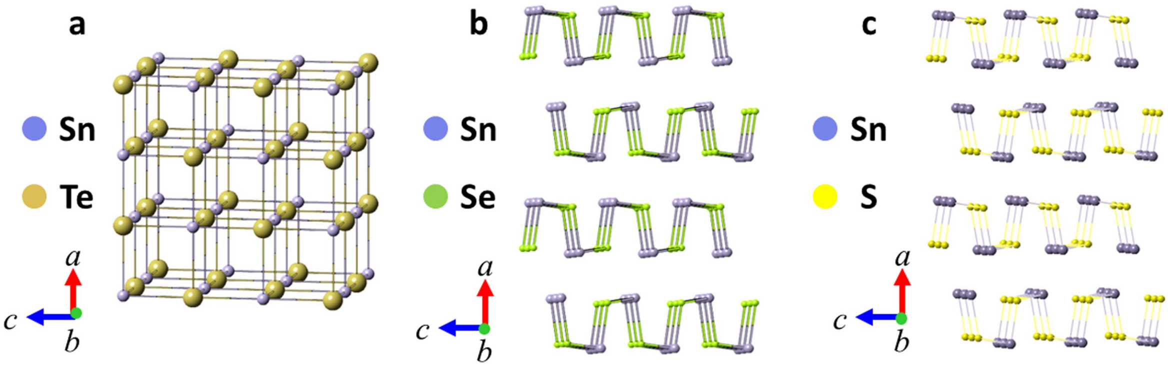

Figure 1. Crystal structure of (a) SnTe in $Fm\bar{3}m$ space group. (b) SnSe in *Pnma* space group. (c) SnS in *Pnma* space group.

which at low temperature could be topological crystalline insulator [21]. A variety of synthetic techniques have been employed to obtain different kinds of SnTe, SnSe and SnS nano-structures such as nanoparticles, nanowires, nanorods, nanosheets. It is reported that SnTe powders can be synthesized by solvothermal method [22, 23], microwave hydrothermal method [24], vapor transport method [25, 26], and solution phase synthesis [27, 28], etc. SnSe powders had been prepared by hydrothermal method [29–31], colloidal synthesis [32], etc. While SnS was obtained by solvothermal method [20]. However, there are still problems, such as the widely used toxic raw materials, the complex reaction conduction, high cost, which have limited the large-scale production.

In this work, we designed a simple, eco-friendly, and cost-efficient hydrothermal route to selectively synthesize SnTe, SnSe and SnS nanopowders, the specific reaction mechanism is discussed in detail. The obtained particles were then compacted by spark plasma sintering (SPS) technique. Then, TE properties were characterized in a wide temperature from 323 to 873 K for SnTe, while SnSe and SnS are measured in two directions, the vertical direction and parallel direction to the pressing direction, from 323 to 773 K. Surprisingly, the ZT value of SnTe reached ~0.79 at 873 K which is the highest value obtained among pristine SnTe samples [16, 33–37]. On the other hand, the ZT values of SnSe and SnS need further enhancement, which may be explored by hydrothermal reaction condition adjustments and doping. This simple hydrothermal approach can be developed to synthesize other binary chalcogenides.

2. Experimental section

2.1. Reagents

$SnCl_2$ powder (99%, Aladdin), Te powders (99.99%, Aladdin), Se powders (99+%, Alfa Aesar), S powders (99.999%, Aladdin), ethylene glycol (EG) (AR), hydrazine hydrate (>98%), NaOH (AR), and deionized (DI) water.

2.2. Synthesis

Powders of polycrystalline SnQ (Q = Te, Se, S) were synthesized by hydrothermal reaction. Firstly, 1 mmol $SnCl_2$ and 3 g NaOH were dissolved in 40 ml DI water after ~10 min stirring to obtain transparent solution as the Sn source. Then, 1 mmol Q (Q = Te, Se, S) powders was dissolved in 20 ml EG after ~10 min stirring, then 15 ml hydrazine hydrate added into the Q (Q = Te, Se, S) solution. After that, $SnCl_2$ solution was slowly dropped into Q (Q = Te, Se, S) containing solution. The entire solution then transferred into a 100 ml PTFE (polytetrafluoroethylene)-lined stainless steel autoclave. The autoclave sealed and heated to 100 °C for 12 h, followed by furnace cooling to room temperature. The black SnQ (Q = Te, Se, S) products were collected by centrifugation and then washed with DI water and ethanol several times before drying under vacuum at 50 °C. The obtained powders then densified to form both disk-shaped and column-shaped bulk samples by SPS (SPS-211Lx, Japan) with an axial pressure of 50 MPa for 5 min, SnTe, SnSe and SnS samples are SPSed at 500 °C, 450 °C and 650 °C, respectively. Due to the texture features, SnSe and SnS are densified to form both disk-shaped and column-shaped bulk samples, and TE properties were characterized in two directions.

2.3. X-ray diffraction (XRD)

The phase structures were investigated by XRD (Rigaku, Tokyo, Japan) at a scanning rate of $4° \text{min}^{-1}$.

2.4. Electrical properties

The obtained SPS processed samples were cut into bars with dimensions 10 mm × 2 mm × 2 mm, the Seebeck coefficient and the electrical resistance were simultaneously measured using an Ulvac Riko ZEM-3 instrument under a helium atmosphere from room temperature to 873 (SnTe) and 773 K (SnSe and SnS). The uncertainty of the Seebeck coefficient and electrical resistance measurements is 5%.

2.5. Thermal conductivity

The thermal conductivity was calculated by $\kappa = DC_p\rho$. Where the thermal diffusivity coefficient (D) was measured using the laser flash diffusivity method in a Netzsch LFA457 (NETZSCH, LFA457, Germany), C_p is the specific heat capacity obtained from previous research [18, 19, 34], and the density (ρ) was determined by the Archimedes method. Considering the uncertainties for D, C_p, and ρ, the uncertainty of the thermal conductivity is estimated to be within 8%, the combined uncertainty for all measurements involved in the calculation of ZT is less than 15%.

2.6. Electron microscopy

Field emission scanning electron microscopy investigation was carried out using ZEISS with operation voltage of 5 kV. Transmission electron microscopy (TEM) investigations were carried out using a FEI Tecnai F30 microscope operated at 300 kV in South University of Science and Technology of China.

2.7. Hall measurement

The Hall coefficients (R_H) were measured by the van der Pauw method on a commercial Hall Effect measurement system (Lake Shore 8400 Series). Hall carrier concentration (n) was then estimated to be equal to $1/eR_H$ and Hall carrier mobility (μ_H) was calculated according to the equation: $\mu_H = R_H\sigma$.

2.8. Band gap measurement

The room temperature optical absorption spectrum was measured using hydrothermal synthesized powders to probe the optical energy gap. The measurement of narrow-band SnTe was performed on Fourier transform infrared spectrometer (Shimadzu, IRAffinity-IS). SnSe and SnS were measured on UV–vis Spectrophotometer (Shimadzu, UV-3600Plus). $BaSO_4$ powder was used as a 100% reflectance standard.

3. Results and discussions

Figure 2 shows the powder x-ray diffraction patterns for SnTe, SnSe, and SnS prepared by the hydrothermal route. All characteristic peaks are well indexed as the low temperature phases, indicating that single phase SnTe, SnSe and SnS were successfully synthesized by a unified hydrothermal method.

The morphology of SnTe, SnSe and SnS powders were characterized in moderate-magnification SEM images shown in figure 3. Figures 3(a) and (b) revealed the octahedron shape of SnTe particles with a diameter ranging from 0.4 to 2.4 μm, and most of the particles are ~0.8 μm. This kind of structure is similar to the product synthesized by microwave hydrothermal method in former report [33]. Figures 3(c) and (d) demonstrated the plate-like features of SnSe with a width ~500 nm and a thickness ~90 nm, and SnSe powders tend to stacked together irregularly. Differently, SnS with plate-like structure formed flower-like secondary particles, as shown in figures 3 (e) and (f). The width and thickness of SnS powders is ~10 μm and ~0.3 μm, respectively.

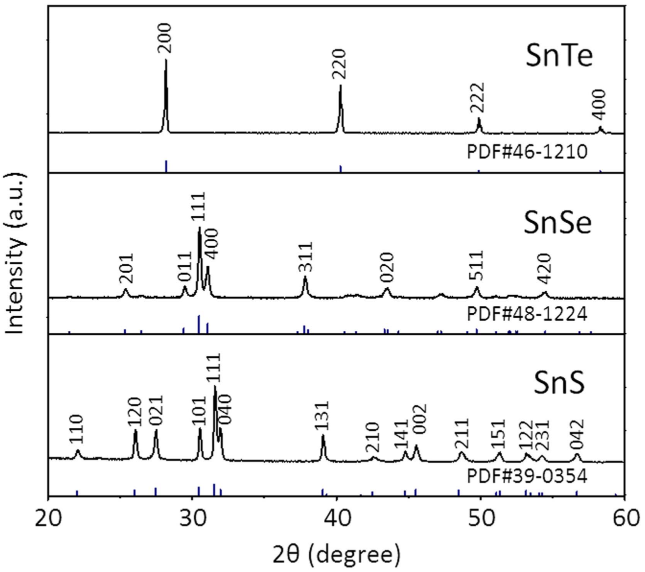

Figure 2. Powder XRD patterns of SnTe, SnSe and SnS.

Moreover, TEM observation was carried out hereby to investigate more details of powders, figure 4. In low-magnification TEM micrographs, the SnTe powders with quadrilateral shadow, SnSe and SnS powders with plate-like shape were obtained, which are consistent with the observation of SEM images. Meanwhile, the high-resolution TEM micrographs with insert of selected area electron diffraction patterns were performed on the thin areas at the edges of the powders. As shown in figures 4(b), (d) and (f), SnTe view along [1 1 0] zone axis, SnSe view along [1 1 2] zone axis and SnS view along [1 0 0] zone axis are clearly characterized, respectively. All these results demonstrate that pristine SnTe, SnSe and SnS powders were successfully synthesized using the simple and unified hydrothermal method.

As shown in figure 5, the schematic diagram of crystal growth mechanism displays the synthetic processes and the features of SnTe, SnSe and SnS powders, respectively. In order to selectively synthesize single phase SnTe, SnSe and SnS powders, an efficient hydrothermal method was employed using $SnCl_2$ as Sn source and elemental Te/Se/S as chalcogen sources. Hydrazine hydrate acted as the reducing agent, DI water and EG were used as the solvents and sodium hydroxide (NaOH) was the pH adjusting agent. The reaction mechanism is consistent for SnTe, SnSe and SnS, which can be explained by the following stepwise chemical reaction equation where we use SnTe as an example:

$$3\mathrm{Te} + 6\mathrm{OH}^- \rightarrow 2\mathrm{Te}^{2-} + \mathrm{TeO_3}^{2-} + 3\mathrm{H_2O}$$

$$\mathrm{TeO_3}^{2-} + \mathrm{N_2H_4} \rightarrow \mathrm{Te} + \mathrm{N_2} \uparrow + \mathrm{H_2O} + 2\mathrm{OH}^-$$

$$\mathrm{Sn}^{2+} + \mathrm{Te}^{2-} \rightarrow \mathrm{SnTe} \downarrow .$$

The optical absorption spectrum of SnTe, SnSe and SnS powders shown in figure 6 reveals the band gap to be 0.21 eV (SnTe), 0.97 eV (SnSe) and 1.07 eV (SnS), respectively, which are consistent with former reports [19, 38, 39].

To further investigate the TE performance of the hydrothermal synthesized SnTe, SnSe and SnS, the corresponding adequately dried powders were then compacted by

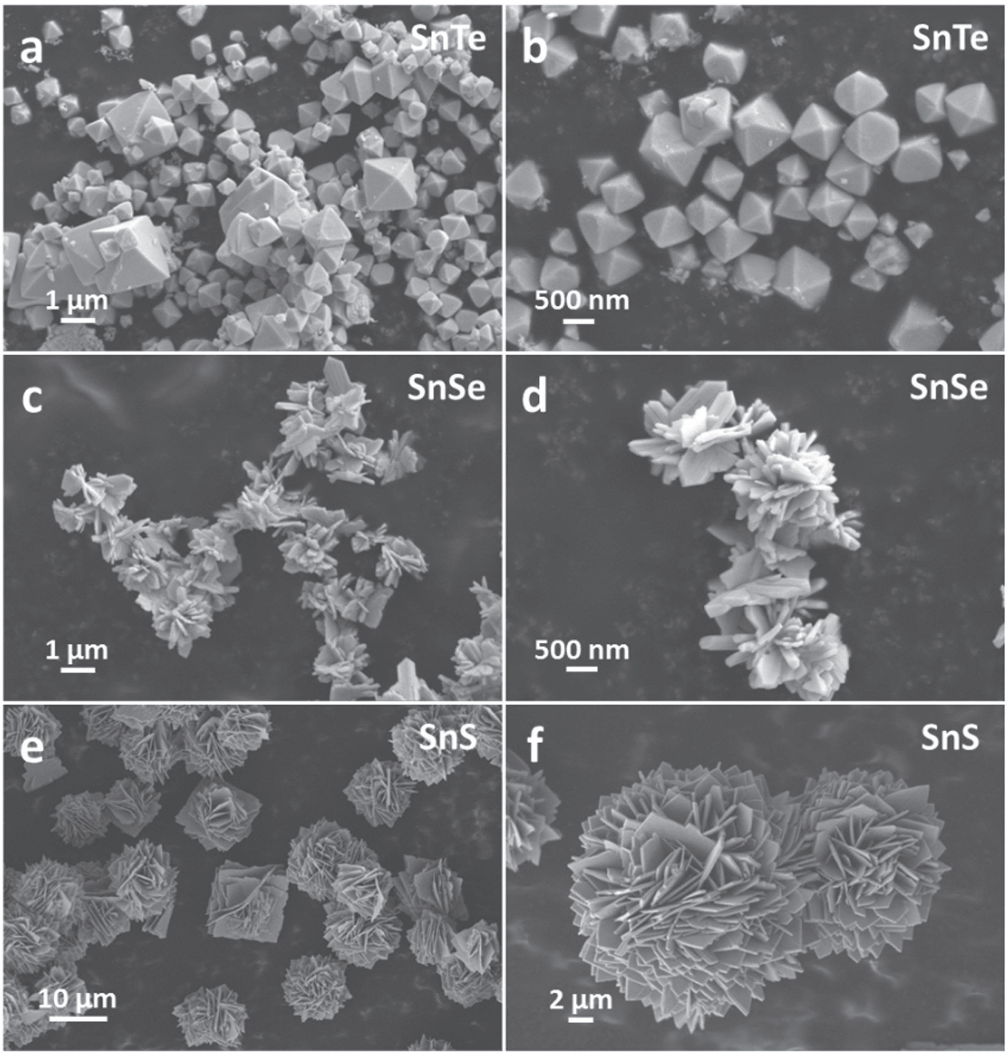

Figure 3. SEM images of (a) and (b) SnTe powders. (c) and (d) SnSe powders. (e) and (f) SnS powders.

SPS at 500 °C, 450 °C and 650 °C refer to previous reports [16, 19, 31]. Figure 7 shows the XRD patterns of bulk samples taken in both the planes vertical and parallel to the pressing direction. As a result, all the characteristic peaks can be well indexed to the crystal planes of the standard JCPDS card files without any second phase peak. Also, it is worth noting that the diffraction intensity of SnSe and SnS shows an obviously difference in the two directions, suggesting the anisotropic feature of SnSe and SnS bulk samples. Specifically, the strongest diffraction peak of SnSe changes from (4 0 0) plane in the vertical direction to (1 1 1) plane in the parallel direction, and the strongest diffraction peak of SnS changes from (0 4 0) plane in the vertical direction to (1 1 1) plane in the parallel direction. The textured phenomenon is mainly attributed to the layered structure of SnSe and SnS crystals, which in 2D form possess unique properties like giant piezoelectricity [40]. Differently, the intensity of diffraction peaks of SnTe is basically the same in two directions due to the cubic structure, suggesting an isotropic feature of SnTe bulk sample.

Figure 8 shows the moderate-magnification SEM micrographs on freshly cleaved surface of bulk SnTe, SnSe and SnS samples, which reveal the microstructure in the planes vertical and parallel to the pressing direction, respectively. As shown in figures 8(a) and (b), no remarkable difference of the morphology was found between two observed directions of SnTe, the grain orientation is isotropic and consistent with the XRD result. Differently, SnSe and SnS were obviously textured during the sintering process, figures 8(c)–(f). The lamellar morphology view along the vertical direction clearly revealed the strong preferential orientation of SnSe and SnS grains. Attributed to the lamellar microstructure in the direction vertical to the pressing direction and strong texture degree, anisotropic transport properties of SnSe and SnS could be expected.

The TE properties including electrical transport properties and thermal conductivities as a function of temperature are displayed in figure 9. The TE properties of SnTe were characterized without distinguish the measurement direction, since the isotropy feature is proved by XRD result and SEM observation, as discussed above. While SnSe and SnS showed strong preferential orientation and anisotropy features, thus the TE properties were measured in different directions, that is, the directions parallel and vertical to the pressing direction.

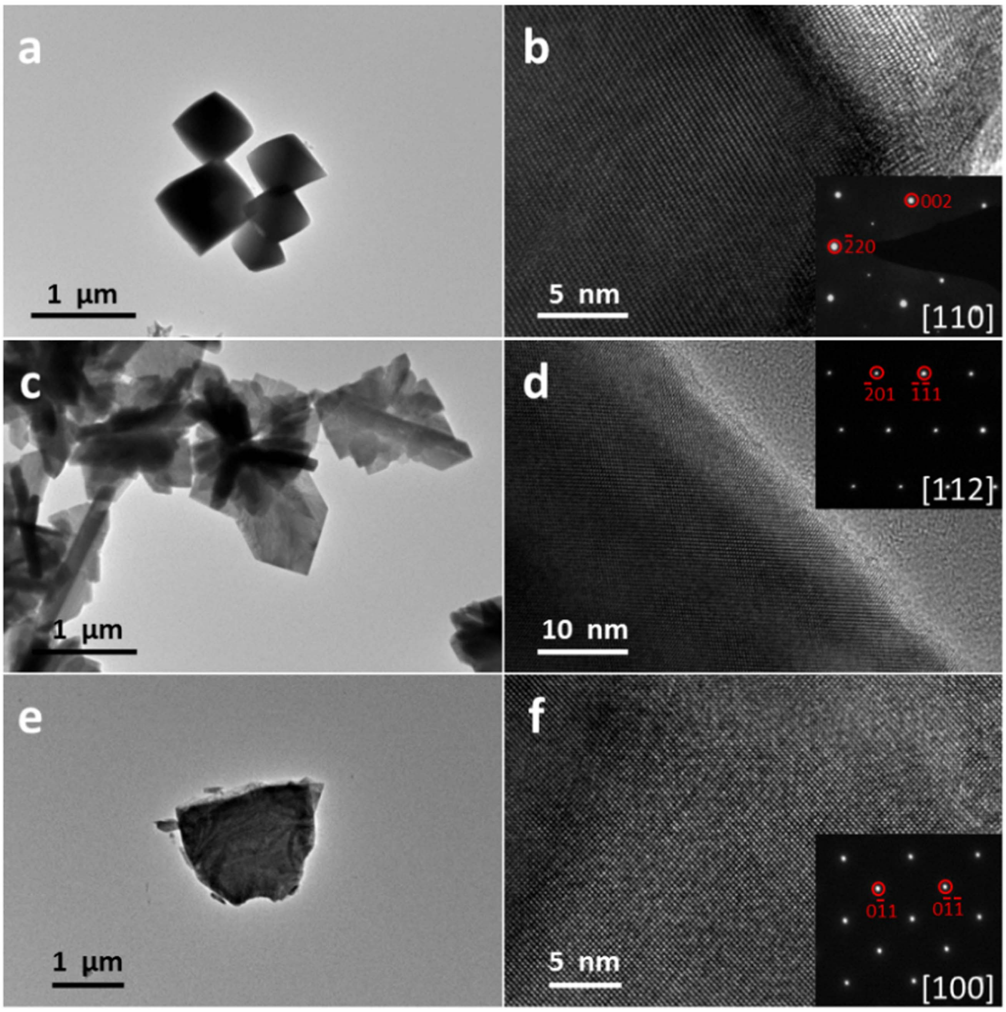

Figure 4. Low-magnification and high-resolution TEM micrographs of (a) and (b) SnTe powders. (c) and (d) SnSe powders. (e) and (f) SnS powders. The inset is the corresponding electron diffraction.

The schematic is inserted in figure 9(a). It is noticed that the sign of the Seebeck coefficient of bulk SnTe, SnSe and SnS samples are positive over the whole temperature range as shown in figure 9(b), evidence a p-type behavior (the dominant charge carrier is hole). The most possible reason is that tin (Sn) is easily volatilized during the sinter process, producing tin vacancies and leading to the generation of positive holes. Thus, we further analyzed the composition of SnTe using Energy dispersive x-ray spectroscopy in SEM. The semi-quantitative analysis result is shown in figure S1 is available online at stacks.iop.org/NANO/28/455707/mmedia, and the absence of tin is confirmed.

As shown in figure 9(a), the electrical conductivity of SnTe (blue line) decreases with increasing temperature over the entire temperature range, indicating a typical metallic behavior. The optical absorption spectrum in figure 6 shows the band gap of SnTe is 0.21 eV, the narrow gap SnTe is degenerate semiconductor. SnTe owns a high carrier concentration ($2.54 \times 10^{20}\,\mathrm{cm}^{-3}$) and Hall mobility ($1.92 \times 10^{2}\,\mathrm{cm}^{2}\,\mathrm{V}^{-1}\,\mathrm{s}^{-1}$), shown in table 1, where the high mobility is attributed to the simple cubic crystal structure which leads to weak carrier scattering, and the high carrier concentration is mainly caused by the volatilization of Sn during the sinter process, figure S1, thus the electrical conductivity and thermal conductivity is extremely high. The electrical conductivity is $\sim$6190 s cm^{-1} at 323 K and decreased to 1690 s cm^{-1} at 873 K, which is slightly lower than the results synthesized by melting method [15, 16, 34–36], but much higher than the best performance sample (sintered from 165 nm nanoparticles) synthesized by microwave hydrothermal method [33]. Meanwhile, the Seebeck coefficient of SnTe increased from 35.4 μVK^{-1} at 323 K to 103 μVK^{-1} at 873 K, which is comparable to the reported data. Attributed to the higher electrical conductivity, the power factor of hydrothermal synthesized SnTe is much higher than the microwave hydrothermal synthesized sample [33]. However, the grain size in this work ($\sim$0.8 μm) is much larger than the microwave hydrothermal synthesized sample ($\sim$165 nm nanoparticles), which is too large to effectively scatter heat-carrying phonons, the weaker phonon scattering thus leads to higher thermal conductivity over the entire temperature range. It is noticed that the thermal diffusivity drops sharply around 623 K, which shows the similar trend with the microwave hydrothermal synthesized sample

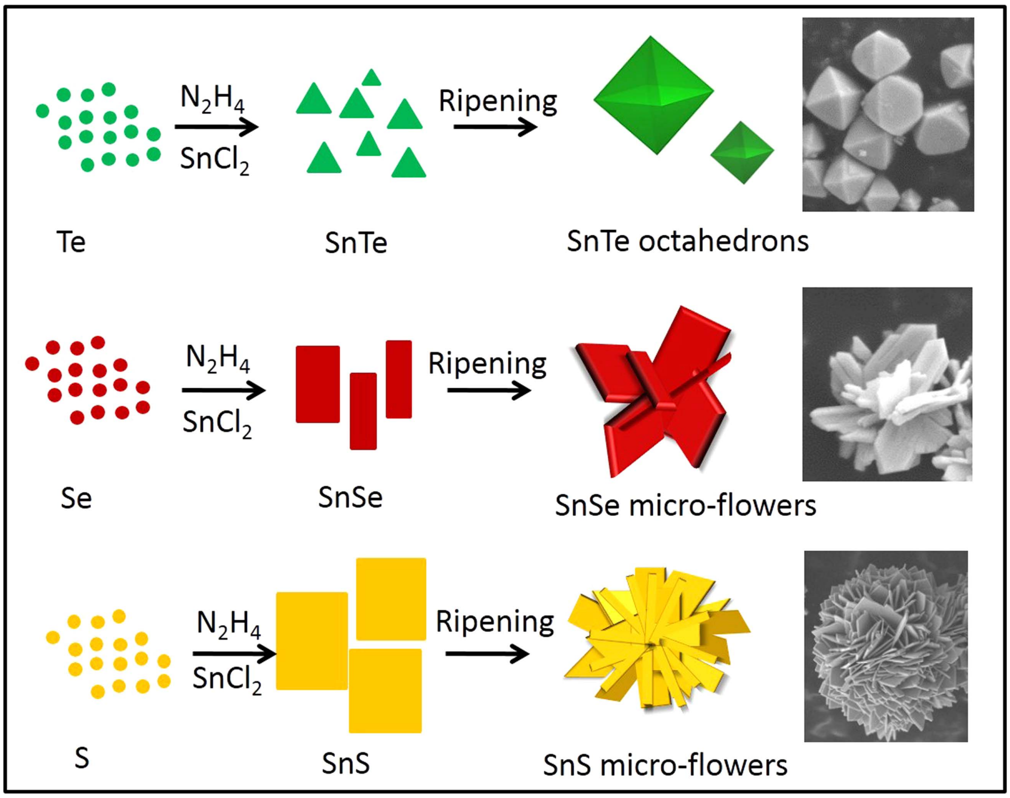

Figure 5. Schematic diagram of the hydrothermal synthetic processes.

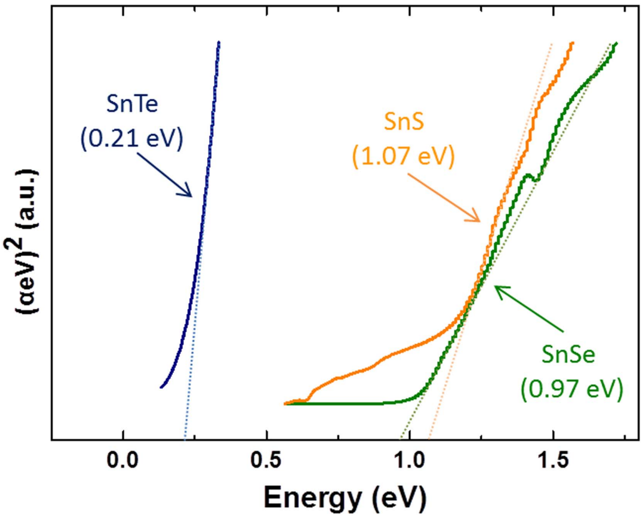

Figure 6. Optical absorption spectrum and energy band gap at room temperature.

sintered from 550 nm particles [33]. To understand this abnormal trend, we re-measured the polished sample with thermal cycling. And this phenomenon was considered to be caused by the surface oxidation and expansion of the sample with the increased temperature during the measurement process. Because the re-measured data of polished sample in the heating process is similar with the original data, but that in the cooling process is not. This issue raised in thermal conductivity measurment process may result in large variation in ZT value. Combining the electrical transport properties and thermal conductivity, the calculated ZT value of pristine SnTe surprisingly reached ~0.79 at 873 K, shown in figure 9(e), which is higher than the microwave hydrothermal synthesized sample and most pristine SnTe samples reported in previous works [16, 33–37].

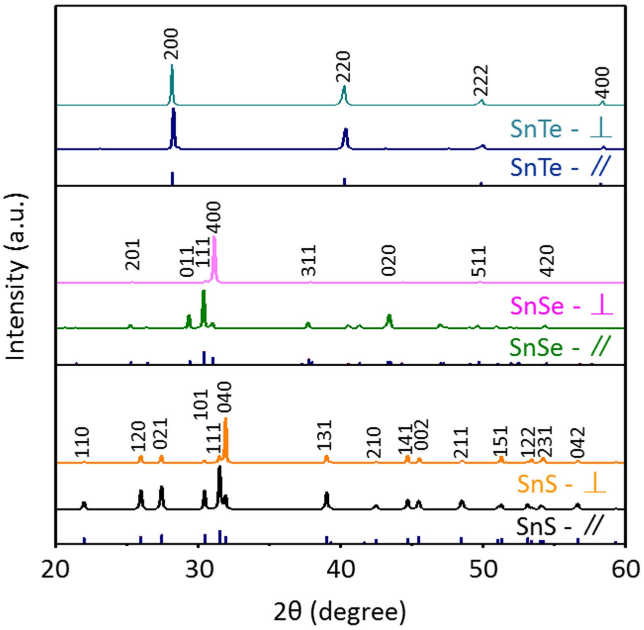

Figure 7. XRD patterns of bulk SnTe, SnSe and SnS samples in the vertical (⊥) and parallel (//) directions.

The XRD results and lamellar morphology shown in SEM micrographs evidence a strong texture in SnSe and SnS

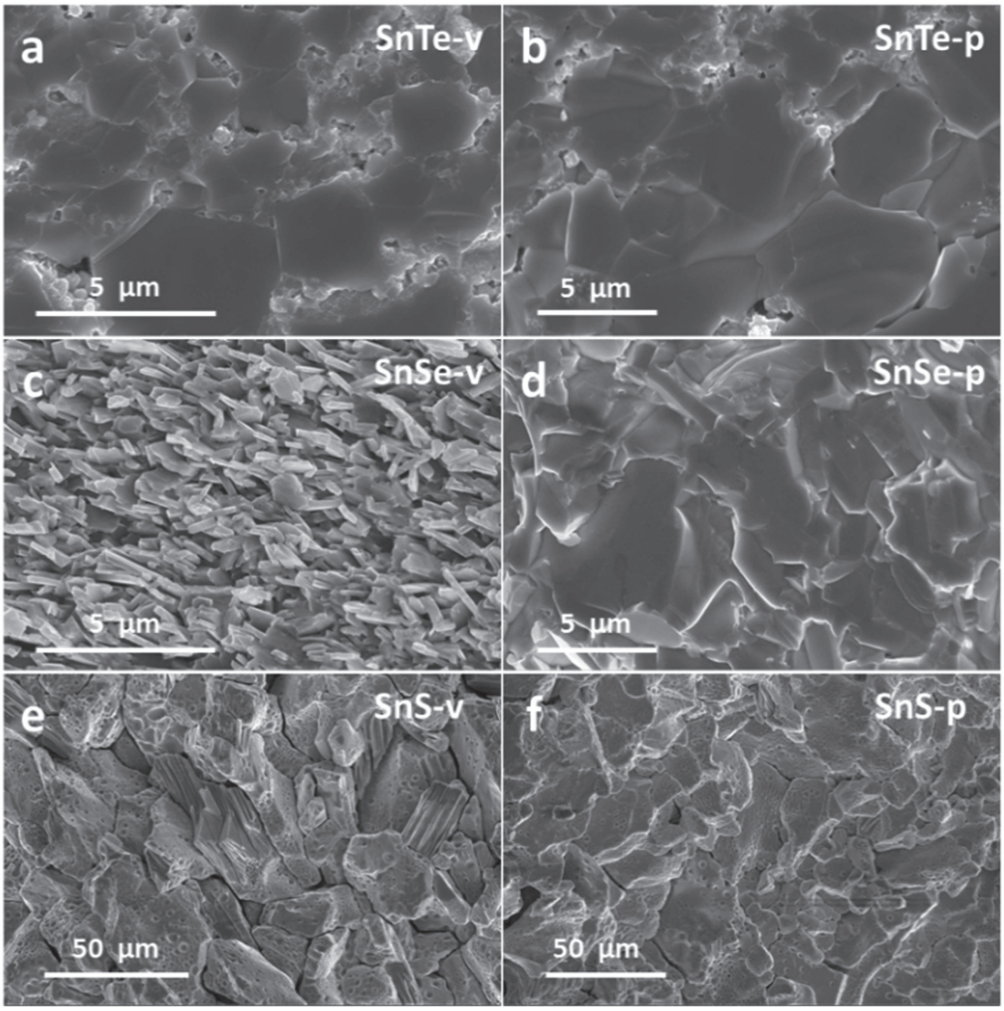

Figure 8. SEM images of bulk (a) and (b) SnTe. (c) and (d) SnSe. (e) and (f) SnS.

bulk samples, the preferential orientation thus lead to a higher mobility in the vertical direction as shown in table 1, especially SnSe, the higher texture degree enlarged the difference of the mobility in two directions, which is clearly reflected in the transport properties, that is, higher electrical conductivity and higher thermal conductivity in the vertical direction.

The electrical conductivity of SnSe (green line) in the vertical direction firstly increased from room temperature to ~573 K, then slightly decreased to ~673 K, and finally upturned at high temperature. This trend is similar to previous reports and well explained by the theory that grain boundary potential barrier scattering dominate the carrier transport in low temperature and phonon scattering mechanism dominate the transport at high temperature [29–31, 41, 42]. However, the maximum electrical conductivity of SnSe is ~32.3 s cm^{-1} in the vertical direction, which is relatively low. Combining with the moderate Seebeck coefficient, the peak power factor ~194 $\mu\mathrm{Wm}^{-1}\,\mathrm{K}^{-2}$ is obtained in the vertical direction at 773 K. The total thermal conductivity consisting of electronic thermal conductivity (κ_e) and lattice thermal conductivity (κ_l) show a decreasing trend over the entire temperature range. The vertical decreases from 0.95 $\mathrm{Wm}^{-1}\,\mathrm{K}^{-1}$ at 323 K to 0.71 $\mathrm{Wm}^{-1}\,\mathrm{K}^{-1}$ at 773 K, and the parallel direction decreases from 5.68 $\mathrm{Wm}^{-1}\,\mathrm{K}^{-1}$ at 323 K to 0.71 $\mathrm{Wm}^{-1}\,\mathrm{K}^{-1}$ at 773 K. Although parallel direction achieves lower thermal conductivity, the vertical direction shows higher ZT value benefiting from the higher power factor. However, the ZT value ~0.21 is not very competitive compared with previous reports.

Similar to SnSe, SnS bulk sample is obviously textured, and shows a higher electrical conductivity and higher thermal conductivity in the vertical direction (orange line). It is noticed that SnS performs higher electrical conductivity in room temperature but owns higher band gap compared with SnSe. This phenomenon is attributed to the more intrinsic defects of SnS caused by the stronger tin (Sn) volatilization, which leads to higher carrier concentration in the room temperature. (Table 1.) Attributed to the extremely low thermal conductivity, the peak ZT value ~0.13 at 773 K is achieved in the parallel direction. Further enhancements of ZT for SnSe and SnS could be expected by reaction condition adjusting, chemical doping, compositing with inorganic nanoparticles, such as SiC, WSe_2 or carbon nano tube, etc.

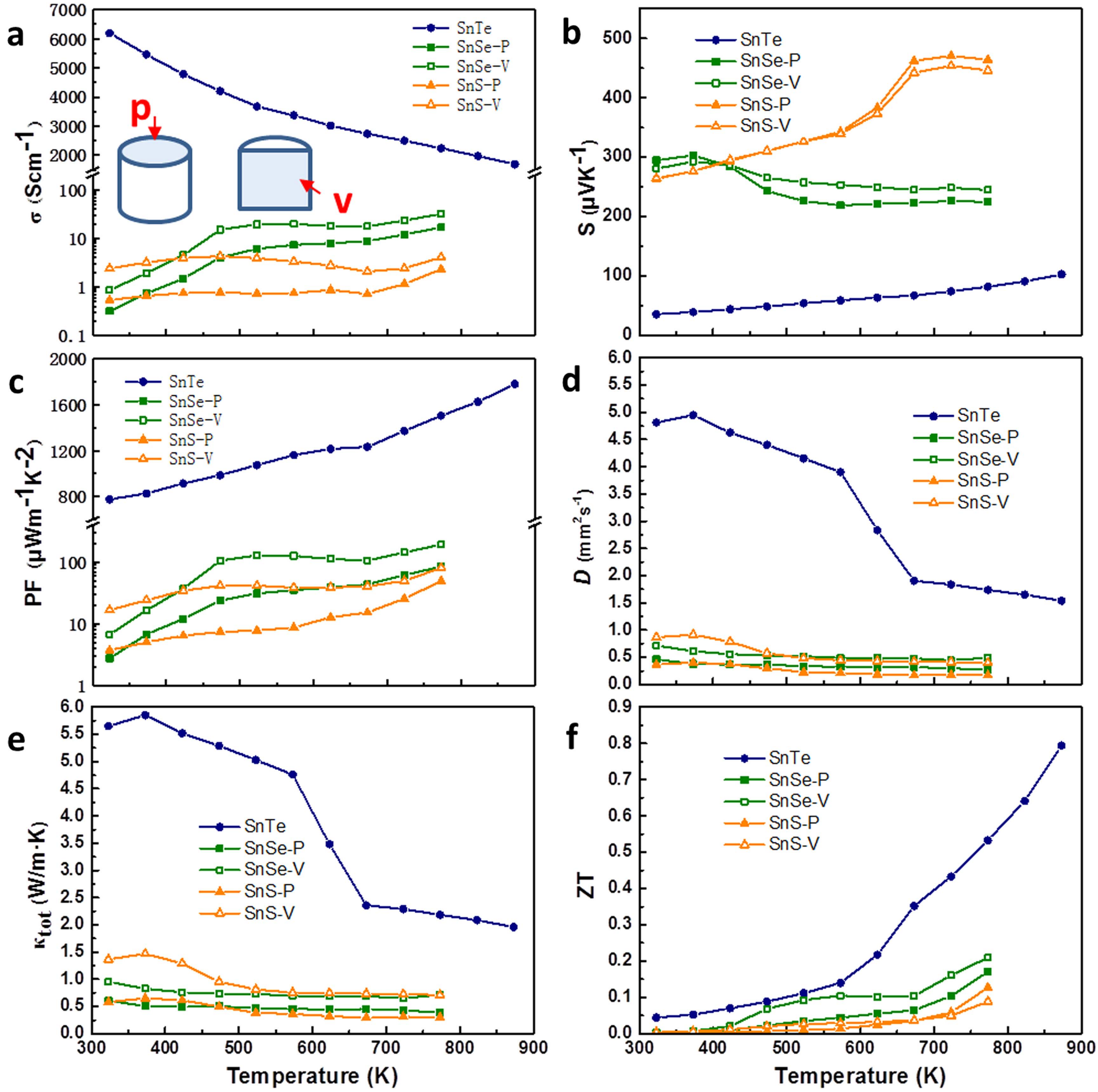

Figure 9. Thermoelectric properties of SnTe, SnSe and SnS: (a) electrical conductivity. (b) Seebeck coefficient. (c) Power factor. (d) Thermal diffusivity. (e) Total thermal conductivity. (e) Figure of merit ZT.

Table 1. Conduction type, carrier concentration and Hall mobility of SnQ (Q = Te, Se and S).

Samples	Conduction type	Carrier concentration (10^{19} cm^{-3})	Hall mobility (cm^2 V^{-1} s^{-1})
SnTe	p	25.4	1.92E2
SnSe-vertical	p	0.509	1.05
SnSe-parallel	p	0.479	4.14E-1
SnS-vertical	p	2.45	6.11E-1
SnS-parallel	p	2.41	1.40E-1

4. Conclusions

In summary, lead-free *IV–VI* semiconductors are promising in TE applications. Pure phase of SnTe, SnSe and SnS particles were successfully synthesized by a simple, eco-friendly, and cost-efficient hydrothermal method with $SnCl_2$ as Sn source and elemental Te/Se/S as chalcogen source. The SnTe particles with octahedron structure and SnSe/SnS particles with plate-like shape were then compacted by SPS. During the sinter process, SnSe and SnS are obviously textured due to the layered structure. The TE properties were characterized, wherein SnSe and SnS were measured in both the vertical and parallel directions. As a result, SnTe achieved a high ZT value ~0.79 at 873 K, while SnSe and SnS need further optimization. This hydrothermal approach can be employed to synthesize other binary chalcogenides, and the reaction conduction can be further optimized.

Acknowledgments

This contribution was supported by the Science, Technology and Innovation Commission of Shenzhen Municipality (KQCX2015033110182370 and JCYJ20150831142508365), Natural Science Foundation of Guangdong Province (Grant No. 2015A030308001), and the leading talents of Guangdong province Program (Grant No. 00201517). JL acknowledges support by NSF DMR-1410636 and ECCS-1610806.

ORCID iDs

Dan Feng https://orcid.org/0000-0002-4104-3424

References

[1] Snyder G J and Toberer E S 2008 Complex thermoelectric materials *Nat. Mater.* **7** 105–14

[2] Sootsman J R, Chung D Y and Kanatzidis M G 2009 New and old concepts in thermoelectric materials *Angew. Chem. Int. Ed.* **48** 8616–39

[3] Heremans J P, Jovovic V, Toberer E S, Saramat A, Kurosaki K, Charoenphakdee A, Yamanaka S and Snyder G J 2008 Enhancement of thermoelectric efficiency in PbTe by distortion of the electronic density of states *Science* **321** 554–7

[4] Pei Y, Shi X, LaLonde A, Wang H, Chen L and Snyder G J 2011 Convergence of electronic bands for high performance bulk thermoelectrics *Nature* **473** 66–9

[5] Pei Y L, Wu H, Wu D, Zheng F and He J 2014 High thermoelectric performance realized in a BiCuSeO system by improving carrier mobility through 3D modulation doping *J. Am. Chem. Soc.* **136** 13902–8

[6] Vineis C J, Shakouri A, Majumdar A and Kanatzidis M G 2010 Nanostructured thermoelectrics: big efficiency gains from small features *Adv. Mater.* **22** 3970–80

[7] He J, Androulakis J, Kanatzidis M G and Dravid V P 2012 Seeing is believing: weak phonon scattering from nanostructures in alkali metal-doped lead telluride *Nano Lett.* **12** 343–7

[8] He J, Zhao L D, Zheng J C, Doak J W, Wu H, Wang H Q, Lee Y, Wolverton C, Kanatzidis M G and Dravid V P 2013 Role of sodium doping in lead chalcogenide thermoelectrics *J. Am. Chem. Soc.* **135** 4624–7

[9] Liu W, Yan X, Chen G and Ren Z 2012 Recent advances in thermoelectric nanocomposites *Nano Energy* **1** 42–56

[10] Biswas K, He J, Blum I D, Wu C I, Hogan T P, Seidman D N, Dravid V P and Kanatzidis M G 2012 High-performance bulk thermoelectrics with all-scale hierarchical architectures *Nature* **489** 414–8

[11] Wang H, Pei Y, LaLonde A D and Snyder G J 2011 Heavily doped p-type PbSe with high thermoelectric performance: an alternative for PbTe *Adv. Mater.* **23** 1366–70

[12] Pei Y, Gibbs Z M, Gloskovskii A, Balke B, Zeier W G and Snyder G J 2014 Optimum carrier concentration in n-type PbTe thermoelectrics *Adv. Energy Mater.* **4** 1400486

[13] Wu H, Carrete J, Zhang Z, Qu Y, Shen X, Wang Z, Zhao L-D and He J 2014 Strong enhancement of phonon scattering through nanoscale grains in lead sulfide thermoelectrics *NPG Asia Mater.* **6** e108

[14] Pei Y, Wang H and Snyder G J 2012 Band engineering of thermoelectric materials *Adv. Mater.* **24** 6125–35

[15] Zhang Q, Liao B, Lan Y, Lukas K, Liu W, Esfarjani K, Opeil C, Broido D, Chen G and Ren Z 2013 High thermoelectric performance by resonant dopant indium in nanostructured SnTe *Natl Acad. Sci. USA* **110** 13261–6

[16] Tan G, Shi F, Hao S, Chi H, Bailey T P, Zhao L D, Uher C, Wolverton C, Dravid V P and Kanatzidis M G 2015 Valence band modification and high thermoelectric performance in SnTe heavily alloyed with MnTe *J. Am. Chem. Soc.* **137** 11507–16

[17] Zhao L-D, Tan G, Hao S, He J, Pei Y, Chi H, Wang H, Gong S, Xu H and Dravid V P 2016 Ultrahigh power factor and thermoelectric performance in hole-doped single-crystal SnSe *Science* **351** 141–4

[18] Zhao L D, Lo S H, Zhang Y, Sun H, Tan G, Uher C, Wolverton C, Dravid V P and Kanatzidis M G 2014 Ultralow thermal conductivity and high thermoelectric figure of merit in SnSe crystals *Nature* **508** 373–7

[19] Tan Q, Zhao L-D, Li J-F, Wu C-F, Wei T-R, Xing Z-B and Kanatzidis M G 2014 Thermoelectrics with earth abundant elements: low thermal conductivity and high thermopower in doped SnS *J. Mater. Chem.* A **2** 17302–6

[20] Tan Q, Wu C-F, Sun W and Li J-F 2016 Solvothermally synthesized SnS nanorods with high carrier mobility leading to thermoelectric enhancement *RSC Adv.* **6** 43985–8

[21] Qian X, Fu L and Li J 2015 Topological crystalline insulator nanomembrane with strain-tunable band gap *Nano Res.* **8** 967–79

[22] Jiang W, Yang Z-L, Weng D, Wang J-W, Lu Y-F, Zhang M-J and Yang Z-Z 2014 Solvothermal synthesis of PbTe/SnTe hybrid nanocrystals *Chin. Chem. Lett.* **25** 849–53

[23] Ning J, Men K, Xiao G, Zou B, Wang L, Dai Q, Liu B and Zou G 2010 Synthesis of narrow band gap SnTe nanocrystals: nanoparticles and single crystal nanowires via oriented attachment *CrystEngComm* **12** 4275

[24] Antunez P D, Buckley J J and Brutchey R L 2011 Tin and germanium monochalcogenide *IV–VI* semiconductor nanocrystals for use in solar cells *Nanoscale* **3** 2399–411

[25] Li Z, Shao S, Li N, McCall K, Wang J and Zhang S X 2013 Single crystalline nanostructures of topological crystalline insulator SnTe with distinct facets and morphologies *Nano Lett.* **13** 5443–8

[26] Safdar M, Wang Q, Mirza M, Wang Z, Xu K and He J 2013 Topological surface transport properties of single-crystalline SnTe nanowire *Nano Lett.* **13** 5344–9

[27] Kovalenko M V, Wolfgang H, Shevchenko E V, Lee J-S, Schwinghammer H, Alivisatos A P and Talapin D V 2007 SnTe nanocrystals: a new example of narrow-gap semiconductor quantum dots *J. Am. Chem. Soc.* **129** 11354–5

[28] Sines I T, Vaughn D D, Biacchi A J, Kingsley C E, Popczun E J and Schaak R E 2012 Engineering porosity into single-crystal colloidal nanosheets using epitaxial nucleation and chalcogenide anion exchange reactions: the conversion of SnSe to SnTe *Chem. Mater.* **24** 3088–93

[29] Li Y, Li F, Dong J, Ge Z, Kang F, He J, Du H, Li B and Li J-F 2016 Enhanced mid-temperature thermoelectric performance of textured SnSe polycrystals made of solvothermally synthesized powders *J. Mater. Chem.* C **4** 2047–55

[30] Ge Z-H, Wei K, Lewis H, Martin J and Nolas G S 2015 Bottom-up processing and low temperature transport properties of polycrystalline SnSe *J. Solid State Chem.* **225** 354–8

[31] Feng D, Ge Z H, Wu D, Chen Y X, Wu T, Li J and He J 2016 Enhanced thermoelectric properties of SnSe polycrystals via texture control *Phys Chem. Chem. Phys.* **18** 31821–7

[32] Liu S, Guo X, Li M, Zhang W H, Liu X and Li C 2011 Solution-phase synthesis and characterization of single-crystalline SnSe nanowires *Angew. Chem. Int. Ed.* **50** 12050–3

[33] Li Z, Chen Y, Li J-F, Chen H, Wang L, Zheng S and Lu G 2016 Systhesizing SnTe nanocrystals leading to thermoelectric performance enhancement via an ultra-fast microwave hydrothermal method *Nano Energy* **28** 78–86

[34] Wu H *et al* 2015 Synergistically optimized electrical and thermal transport properties of SnTe via alloying high-solubility MnTe *Energy Environ. Sci.* **8** 3298–312

[35] Tan G, Zhao L D, Shi F, Doak J W, Lo S H, Sun H, Wolverton C, Dravid V P, Uher C and Kanatzidis M G 2014 High thermoelectric performance of p-type SnTe via a synergistic band engineering and nanostructuring approach *J. Am. Chem. Soc.* **136** 7006–17

[36] Tan G, Shi F, Sun H, Zhao L-D, Uher C, Dravid V P and Kanatzidis M G 2014 SnTe–$AgBiTe_2$ as an efficient thermoelectric material with low thermal conductivity *J. Mater. Chem.* A **2** 20849–54

[37] Chen Y, Nielsen M D, Gao Y-B, Zhu T-J, Zhao X and Heremans J P 2012 SnTe–$AgSbTe_2$ thermoelectric alloys *Adv. Energy Mater.* **2** 58–62

[38] Zhang Q, Chere E K, Sun J, Cao F, Dahal K, Chen S, Chen G and Ren Z 2015 Studies on thermoelectric properties of n-type polycrystalline $SnSe_{1-x}S_x$ by iodine doping *Adv. Energy Mater.* **5** 1500360

[39] Rogers L M 2002 Valence band structure of SnTe *J. Phys. D: Appl. Phys.* **1** 845

[40] Fei R, Li W, Li J and Yang L 2015 Giant piezoelectricity of monolayer group IV monochalcogenides: SnSe, SnS, GeSe, and GeS *Appl. Phys. Lett.* **107** 173104

[41] Chen C-L, Wang H, Chen Y-Y, Day T and Snyder G J 2014 Thermoelectric properties of p-type polycrystalline SnSe doped with Ag *J. Mater. Chem.* A **2** 11171

[42] Wei T R, Wu C F, Zhang X, Tan Q, Sun L, Pan Y and Li J F 2015 Thermoelectric transport properties of pristine and Na-doped $SnSe_{1-x}Te_x$ polycrystals *Phys. Chem. Chem. Phys.* **17** 30102–9